Article

Giant nonlinear optical responses from photon-avalanching nanoparticles

https://doi.org/10.1038/s41586-020-03092-9

Received: 10 July 2020

Accepted: 17 November 2020

Published online: 13 January 2021

Check for updates

Changhwan Lee[1], Emma Z. Xu[1], Yawei Liu[2,3], Ayelet Teitelboim[2], Kaiyuan Yao[1], Angel Fernandez-Bravo[2,8,9], Agata M. Kotulska[4], Sang Hwan Nam[5], Yung Doug Suh[5,6]✉, Artur Bednarkiewicz[4]✉, Bruce E. Cohen[2,7]✉, Emory M. Chan[2]✉ & P. James Schuck[1]✉

Avalanche phenomena use steeply nonlinear dynamics to generate disproportionately large responses from small perturbations, and are found in a multitude of events and materials[1]. Photon avalanching enables technologies such as optical phase-conjugate imaging[2], infrared quantum counting[3] and efficient upconverted lasing[4–6]. However, the photon-avalanching mechanism underlying these optical applications has been observed only in bulk materials and aggregates[6,7], limiting its utility and impact. Here we report the realization of photon avalanching at room temperature in single nanostructures—small, Tm^{3+}-doped upconverting nanocrystals—and demonstrate their use in super-resolution imaging in near-infrared spectral windows of maximal biological transparency. Avalanching nanoparticles (ANPs) can be pumped by continuous-wave lasers, and exhibit all of the defining features of photon avalanching, including clear excitation-power thresholds, exceptionally long rise time at threshold, and a dominant excited-state absorption that is more than 10,000 times larger than ground-state absorption. Beyond the avalanching threshold, ANP emission scales nonlinearly with the 26th power of the pump intensity, owing to induced positive optical feedback in each nanocrystal. This enables the experimental realization of photon-avalanche single-beam super-resolution imaging[7] with sub-70-nanometre spatial resolution, achieved by using only simple scanning confocal microscopy and without any computational analysis. Pairing their steep nonlinearity with existing super-resolution techniques and computational methods[8–10], ANPs enable imaging with higher resolution and at excitation intensities about 100 times lower than other probes. The low photon-avalanching threshold and excellent photostability of ANPs also suggest their utility in a diverse array of applications, including sub-wavelength imaging[7,11,12] and optical and environmental sensing[13–15].

The primary advantage of photon avalanching (PA) is its combination of extreme nonlinearity and efficiency, achieved without any periodic structuring or interference effects. PA was first observed over 40 years ago in Pr^{3+}-doped bulk crystals, which exhibited a sudden increase in upconverted luminescence when excited beyond a critical pump laser intensity[3]. Its discovery quickly led to the development of other lanthanide-based bulk PA materials—used, for example, in efficient upconverted lasers[4–6,16]—and its unique properties continue to spark interest over diverse fields[6,7].

PA is a positive-feedback system[6] analogous to the second-order phase transition of ferromagnetic spin systems—a comparison that has proved to be useful for modelling the process[5,17]. In lanthanide-based PA, a single ground-state absorption (GSA) event initiates a chain reaction of excited-state absorption (ESA) and cross-relaxation events between lanthanide (Ln^{3+}) ions, resulting in the emission of many upconverted photons (Fig. 1a and Methods). The sensitivity of Ln^{3+} photophysics to local material properties has precluded the realization of PA in nanomaterials. Avalanche-like behaviour in previous nanoparticle designs was ultimately the result of the formation of larger aggregate materials[18], non-PA thermal mechanisms[19,20] or pre-avalanche energy looping[6,11,13,21–27], with nonlinear order s ranging from 2 to 7 (s is defined by $I_e = I_p^s$, where I_e is the emission intensity and I_p is the pump intensity)[7,11,22]. There remains strong motivation for developing PA in nanoparticles, given that the ability to process these colloidal

[1]Department of Mechanical Engineering, Columbia University, New York, NY, USA. [2]The Molecular Foundry, Lawrence Berkeley National Laboratory, Berkeley, CA, USA. [3]State Key Laboratory of Rare Earth Resource Utilization, Changchun Institute of Applied Chemistry, Chinese Academy of Sciences, Changchun, China. [4]Institute of Low Temperature and Structure Research, Polish Academy of Sciences, Wroclaw, Poland. [5]Laboratory for Advanced Molecular Probing (LAMP), Korea Research Institute of Chemical Technology (KRICT), DaeJeon, South Korea. [6]School of Chemical Engineering, Sungkyunkwan University (SKKU), Suwon, South Korea. [7]Division of Molecular Biophysics and Integrated Bioimaging, Lawrence Berkeley National Laboratory, Berkeley, CA, USA. [8]Present address: SUPA, School of Physics and Astronomy, University of St Andrews, St Andrews, UK. [9]Present address: Centre of Biophotonics, University of St Andrews, St Andrews, UK. ✉e-mail: ydsuh@krict.re.kr; a.bednarkiewicz@intibs.pl; becohen@lbl.gov; emchan@lbl.gov; p.j.schuck@columbia.edu

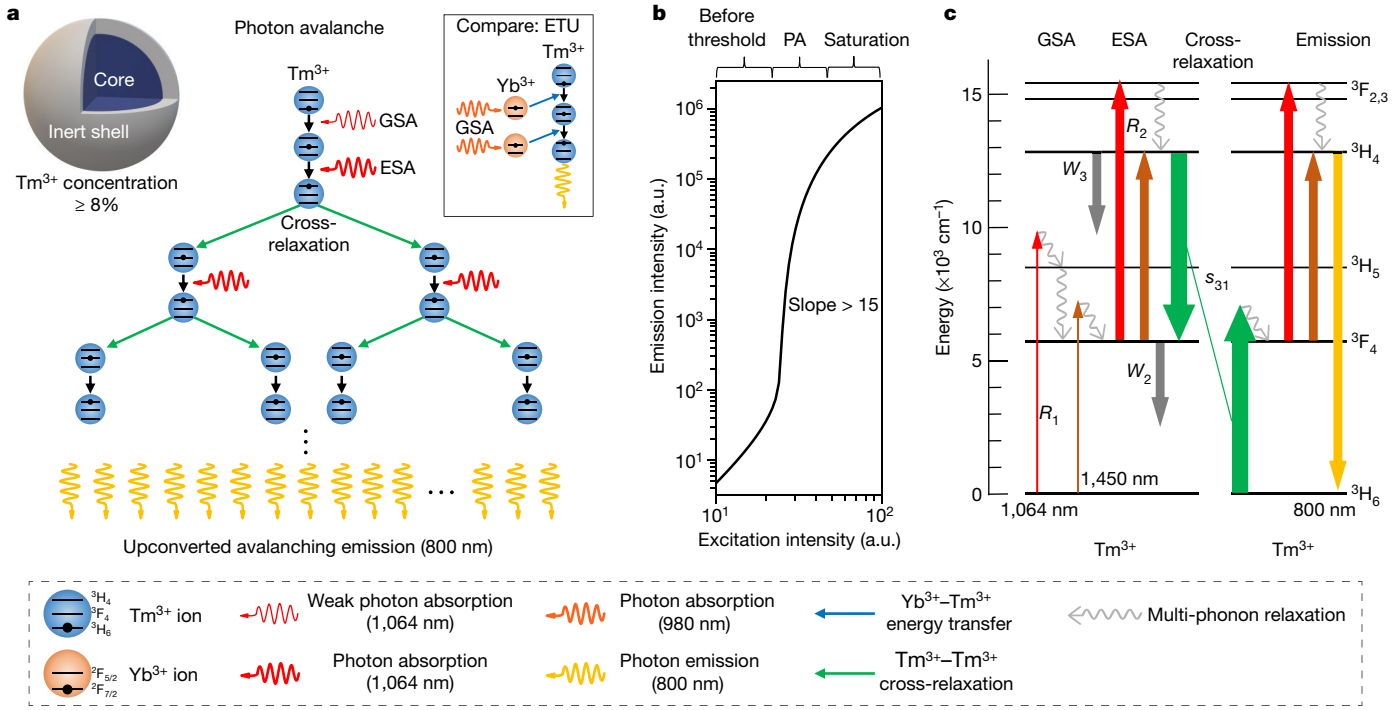

Fig. 1 | PA mechanism in Tm^{3+}-doped nanocrystals. a, Core–shell ANPs, with avalanching occurring when the core Tm^{3+} concentration is ≥8%. Inset, standard energy-transfer upconversion (ETU) process, in which Yb^{3+} ions sensitize ground-state absorption, precluding PA. **b**, Model plot of emission intensity versus excitation intensity, showing the three stages of PA behaviour. **c**, Energy levels of the $4f^{12}$ manifolds of Tm^{3+} and their transitions. R_1 and R_2 denote the ground- and excited-state excitation rates, respectively. W_2 and W_3 are the aggregate rates of relaxation from the $^3F_4$ and $^3H_4$ levels, respectively. These rates account for radiative and non-radiative relaxation pathways but exclude cross-relaxation and other energy-transfer processes. s_{31}, cross-relaxation rate; a.u., arbitrary units.

nanomaterials in solution allows them to be incorporated into various device platforms, nanotechnologies and environments[23,28], using biocompatible surface chemistries[28–31] and materials[32].

To design nanocrystals that may be capable of PA, we combined four key elements: (1) the recent design paradigm for upconverting nanoparticles, which emphasizes high Ln^{3+} content and energy confinement[23,29,33–37]; (2) the choice of Tm^{3+} (Fig. 1a), with its slow intermediate-state decay rate W_2; (3) compositions that omit sensitizers[22] (for example, Yb^{3+} in Fig. 1a, inset); and (4) the selection of excitation wavelengths in the second near-infrared window (NIR-II) (either 1,064 nm or 1,450 nm; Fig. 1c) optimized for resonant ESA, in contrast to the usual Tm^{3+} ground-state pumping wavelengths (800 nm, or 980 nm with Yb^{3+} sensitization; Fig. 1)[6,11,12,21,38]. These design specifications enabled us to synthesize Tm^{3+}-doped β-$NaYF_4$ core–shell structures 16–33 nm in total diameter[29,33] (Methods; Supplementary Figs. 1, 2; and Supplementary Tables 1, 2), which are excited in the NIR-II region and emit in the NIR-I region at 800 nm (ref. [22]).

To determine whether PA occurs, we examined the nanoparticles for three definitive criteria[5,6]: (i) stronger pump-laser-induced ESA compared to GSA, with the ratio of ESA to GSA rates exceeding 10^4 (R_2/R_1 in Fig. 1c)[22]; (ii) a clear excitation-power threshold, above which a large nonlinear increase in excited-state population and emission is observed; and (iii) a slowdown of the excited-state population rise time at threshold. For PA, rise times typically reach more than 100 times the lifetime of the intermediate state, up to seconds[6]. Together, these criteria delineate PA from other nonlinear multiphoton processes, including conventional energy-transfer upconversion (Fig. 1a inset) and energy looping[22].

Plots of Tm^{3+} emission at 800 nm versus 1,064 nm pump intensity measured on nanoparticle ensembles drop-casted onto glass substrates show that as Tm^{3+} content is increased from 1% to 4%, the degree of nonlinearity s also increases, but resides firmly in the energy looping regime, with $s \leq 7$ (Fig. 2a). At these Tm^{3+} concentrations, the chain reaction of ESA and cross-relaxation is too slow to compensate for radiative and multiphonon relaxation from the $^3F_4$ intermediate state, which occurs with a rate of W_2. However, at 8% Tm^{3+} doping, a clear threshold is observed at pump intensity of about 20 kW cm^{-2} (Supplementary Fig. 3 and Table 3), beyond which the combination of cross-relaxation and ESA act as a gain, and a nonlinear slope of $s > 22$ is achieved (Fig. 2a, grey circles), surpassing the maximum value of 7 observed in the existing pre-avalanching systems. Up- and down-scans of excitation intensity display no measurable photobleaching nor hysteresis, thus showing no detectable contribution from excitation-induced thermal avalanching (Supplementary Information Fig. 4)[39]. Critically, all three PA criteria are met at room temperature for these 8% Tm^{3+} ANPs (Fig. 2).

To understand why 8% Tm^{3+} doping gives rise to such nonlinear emission, we modelled the PA process in ANPs using coupled nonlinear differential rate equations[17,40] (DREs; see Supplementary Information and Supplementary Tables 4–8). Fitting the model to the experimental data for 8% Tm^{3+} ANPs (Fig. 2a, grey dash-dotted line) yields an ESA-to-GSA rate (R_2/R_1) ratio of more than 10,000 (Supplementary Table 6), satisfying the $R_2/R_1 > 10^4$ criterion for PA[6,41].

To observe the signature slow-down in the excited-state population rise times expected for PA[4,6,17,42], time-dependent luminescence from the Tm^{3+} $^3H_4$ level (800 nm emission) was measured (Fig. 2b; Methods and Supplementary Figs. 6–8). The rise time is defined as the time needed to reach 95% of the asymptotic value (Supplementary Fig. 7). We observe that a substantial lengthening of the luminescence rise time emerges near the PA threshold intensity, reaching a maximum of approximately 608 ms (Fig. 2b)—nearly 400 times the lifetime of the $^3F_4$ state—further verifying that the PA mechanism prevails in these nanoparticles.

Our modelling also predicts PA for even longer-wavelength excitation near 1,450 nm, resonant with ESA between $^3F_4$ and $^3H_4$, but not with GSA (Fig. 1c). This is a technologically attractive wavelength range because

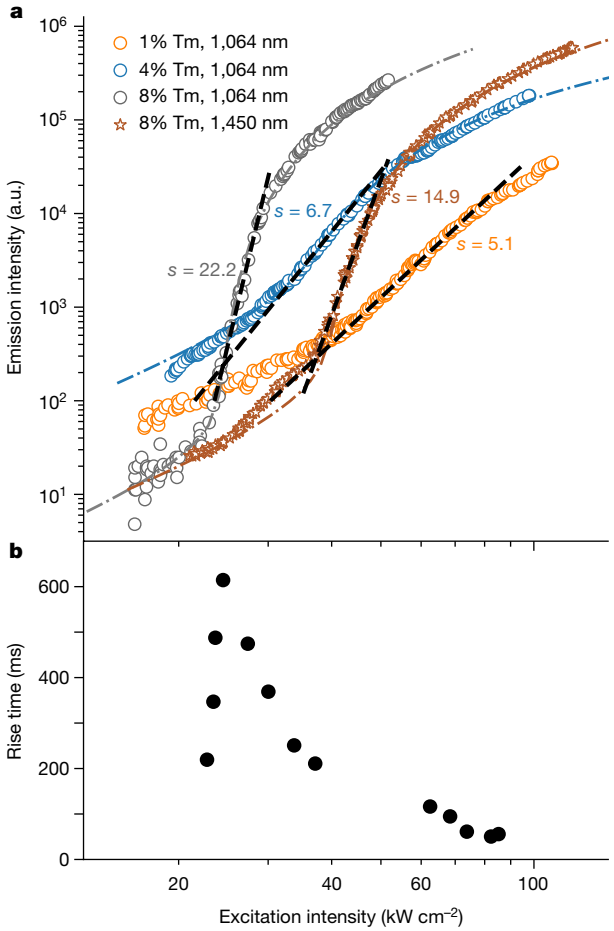

Fig. 2 | Demonstration of nanoparticle PA. a, 800-nm emission intensity versus excitation intensity for ensemble films of 1%, 4% and 8% Tm^{3+}-doped nanocrystals. Excitation at 1,064 nm excitation is used, except where noted. See Supplementary Tables 1, 2 for ANP sizes. PA is also achieved in the 8% Tm^{3+} ANPs with 1,450 nm excitation (brown stars). The dash-dotted lines are fits of the PA DRE model to the data, as described in the text and the Supplementary Information. **b**, 800-nm emission rise times versus excitation intensity for the 8% Tm^{3+} ANPs in **a**, showing a large increase, up to 608 ms, near the PA threshold.

it is beyond the absorption cut-off of Si-based detectors and leads to emission that is easily detected by Si, and is also useful for deep-tissue imaging, including through-skull fluorescence imaging of live mouse brain at depths greater than 2 mm (ref. [43]). Using 1,450-nm excitation, we indeed observe PA, with the emission–intensity curve showing a threshold at about 40 kW cm^{-2} and a maximum nonlinearity of $s = 14.9$ (Fig. 2a, brown stars). More generally, the ANPs demonstrate PA for wavelengths between 1,400 nm and 1,470 nm (Supplementary Fig. 9), with the lowest threshold occurring at 1,450 nm in this range.

Recent theoretical treatments show that achieving PA with a large nonlinearity involves a complex balance between several coexisting phenomena within the material[7]. However, in the limiting case in which the cross-relaxation rate s_{31} is much greater than W_2, the DRE model predicts that threshold intensity is determined entirely by W_2 (refs. [5,17]). In ANPs, s_{31} is controlled by the Ln^{3+} concentration, whereas the non-radiative decay component of W_2 is dominated by losses at surfaces and interfaces[29,34,35,44,45]. To determine whether rebalancing these factors would reduce threshold intensity, we synthesized two 8% Tm^{3+} core–shell structures designed to reduce surface losses, and thus W_2. These designs include thicker shells, as well as larger core size than the 8% ANPs in Fig. 2, to further reduce the surface-to-volume ratio. The changes indeed result in a distinct reduction in threshold, to <10 kW cm^{-2} at room temperature (Fig. 3a, Supplementary Fig. 5).

We further hypothesized that increasing the Tm^{3+} content should change s_{31} and W_2, and therefore the PA excitation threshold intensity. To study this effect, core–shell ANPs with 20% and 100% Tm^{3+} were synthesized (including two sizes of 20% Tm^{3+} ANPs; Supplementary Fig. 1), and the threshold intensity was found to increase with increasing Tm^{3+} content (Fig. 3a). This is consistent with recent studies showing that at these pump intensities, excited-state lifetimes are reduced (W_2 is increased) as Ln content increases within nanoparticles, with the resulting increase in ion–ion energy transfer opening many potential relaxation pathways that act collectively to depopulate and repopulate the levels[29,46].

Models predict a linear dependence between PA threshold intensity and W_2, with a slope that is determined by s_{31}, W_3 (the excited-state decay rate; see Fig. 1c) and the excited-state relaxation branching ratio[5,17]. These dependencies are shown in Fig. 3b for three different Tm^{3+} concentrations. As s_{31} increases, W_3 and the branching ratio become less important, leading to a slight reduction in slope in the threshold-intensity–W_2 curves. The presence of the 20% and 100% Tm^{3+} data points on nearly the same line demonstrates that by the time the Tm^{3+} content reaches 20%, s_{31} dominates, and the relative effects of W_3 and the branching ratio become almost negligible. This well defined relationship between the PA threshold and W_2 shown in Fig. 3b has important implications for sensing applications, in which W_2 can be modulated by environmentally dependent energy transfer to the ANP surface, with small changes in W_2 (and thus threshold) resulting in large changes in luminescence for a given pump intensity.

To evaluate the efficiency and relative brightness of ANPs, we used a kinetic computational model of energy transfer within Ln^{3+}-doped nanoparticles, similar to those used to reproduce the experimental upconverting quantum yields of Er^{3+}/Yb^{3+}co-doped upconverting nanoparticles[33,47], as well as energy-looping nanoparticles[22] (Supplementary Information). Our calculations reveal that for fully passivated core–shell nanoparticles, the quantum yield can reach about 40% for ANPs excited beyond the threshold at 10^5 W cm^{-2} (Fig. 3c). Although the model has known limitations—in particular, the absence of higher-energy excited states—we note that calculated quantum yields are consistent with both previous quantum yield calculations for energy-looping nanoparticles[22] and quantum yield measurements of PA-induced upconversion in fibres at room temperature[16]. In our calculations, we find that whereas the 8% Tm^{3+} ANPs are somewhat more efficient than the 20% ANPs at this pump fluence, the 20% ANPs are brighter (Fig. 3c). This is because brightness is a function of quantum yield, but also of the total number of emitters within the ANP (brightness is defined as the product of the wavelength-dependent Tm^{3+} ion absorption cross-section, the Tm^{3+} concentration and the quantum yield). The emission intensity shows a more nonlinear dependence on pump fluence than does quantum yield, given that the extreme nonlinearity of PA emission is a function of both intensity-dependent quantum yield and excited-state populations.

A compelling application for ANPs is single-particle super-resolution imaging, as elucidated by the recently proposed photon-avalanche single-beam super-resolution imaging (PASSI) concept, which exploits the extreme nonlinear response of PA[7]. The size of the imaging point spread function in scanning confocal microscopy (SCM) scales inversely with the square root of the degree of nonlinearity s (as in multiphoton microscopy)[7], with the full-width at half-maximum (FWHM) of an imaged nonlinear emitter in SCM given by:

$$\mathrm{FWHM} = \frac{\lambda}{2\mathrm{NA}\sqrt{s}}$$

in the Gaussian optics approximation[48] (where NA is the numerical aperture and λ is the wavelength). Therefore, deeply sub-wavelength

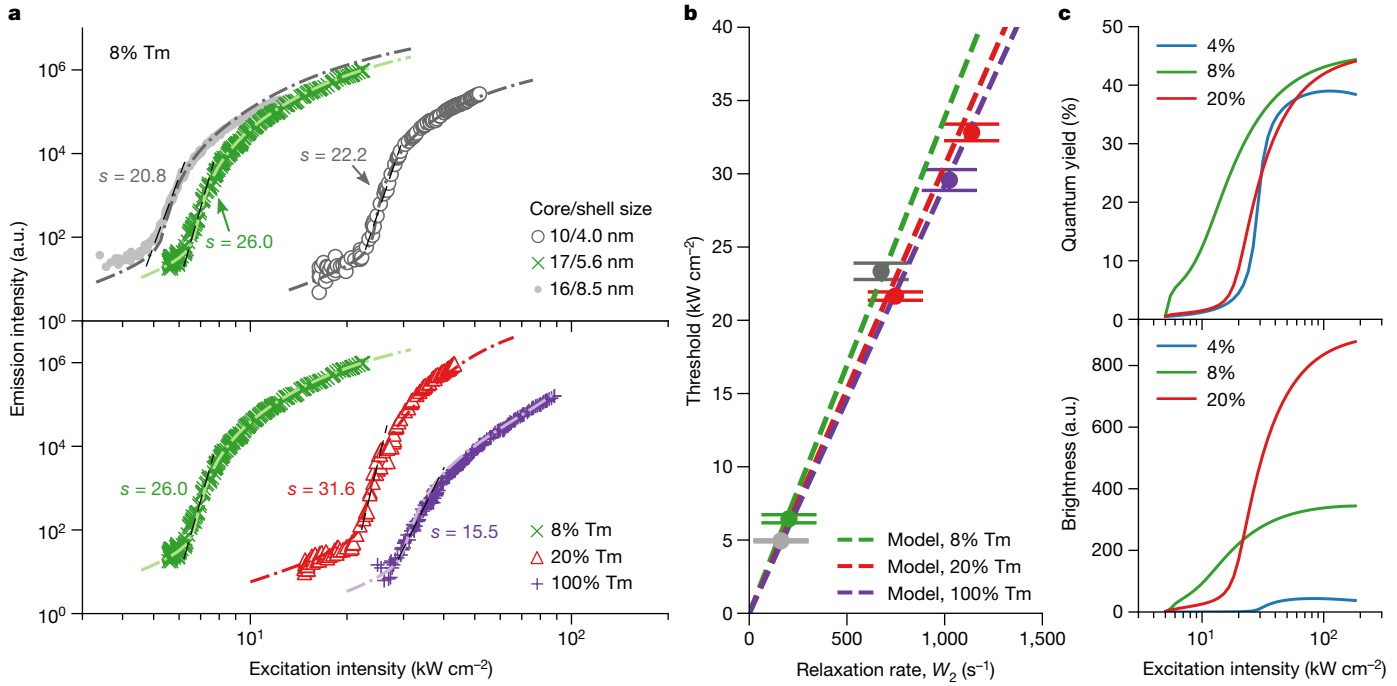

Fig. 3 | Modifying PA kinetics via ANP shell thickness, surface-to-volume ratio and Tm^{3+} content. a, Top, 800-nm emission intensity versus 1,064-nm excitation intensity curves for different core sizes and shell thicknesses of 8% Tm^{3+}-doped ANPs. Bottom, ANPs with different Tm^{3+} concentrations. Green × symbols: 8% Tm^{3+}, same as top panel. Red triangles: 20% Tm^{3+} (see Supplementary Information for sample details; data for sample 7 are shown; the curve for sample 6 with 20% Tm^{3+} is shown in Supplementary Figs. 3, 5). Purple + symbols: 100% Tm^{3+}. See Supplementary Tables 1, 2 for measured dimensions and their standard deviations. The dash-dotted lines are fits of the PA DRE model to the data. All measurements were performed on ensemble films. **b**, Threshold intensity versus W_2, extracted from the data in **a**, showing linear dependencies on W_2, with slopes that depend on s_{31}. Error bars are determined from the standard deviations of the curve fittings shown in Supplementary Fig. 3. **c**, **d**, Calculations of upconverting quantum yield (**c**) and brightness (**d**) versus excitation intensity for 4%, 8% and 20% Tm^{3+}, using values from model fits to the green circles and red squares in **a**, and the blue circles in Fig. 2a.

resolution would be realized automatically with ANPs during standard SCM. The imaging requires no complex instrumentation, excitation beam shaping or patterning, image post-processing, or alignment procedures[7].

We performed single-ANP imaging, measuring a PASSI image spot of ≤75 nm average FWHM when excited at 1,064 nm at the optimal pump intensity for PASSI, which corresponds to emission intensity at the top of the steep segment of the response curve[7] (see Methods). More specifically, the image of the 8% Tm^{3+} ANP from the batch with $s = 26$ (Fig. 3a), shows a short-axis FWHM of 65 ± 7 nm and a long-axis FWHM of 81 ± 9 nm (Fig. 4b and Supplementary Fig. 10), with its elliptical shape due to a slightly elliptical excitation spot. This spot size agrees well with PASSI simulations (Fig. 4e). The comparison with a diffraction-limited excitation spot size of 357 nm FWHM clearly shows the advantage of the extreme nonlinearity of PA (Fig. 4c). In Fig. 4a, the spot size is ~220 nm FWHM when excited closer to the saturation regime, where the degree of nonlinearity s is considerably lower, as predicted[7] (Fig. 4d). The theoretical resolution limit considering $s = 26$ is 70 nm, in excellent agreement with the measured values. PASSI super-resolution and its unique power dependence is readily apparent, with two ANPs separated by 300 nm being just resolvable when excited near saturation, but easily resolvable for intensities in the steep-slope region of the PA emission–pump intensity curve (Fig. 4g, h). The resolution is fully determined by the slope of the power-dependent emission (Fig. 4f) curve, allowing us to select the optimal intensity for imaging for a given ANP architecture once that curve is measured[7]. Beyond PASSI, there are also notable advantages for combining the steeply nonlinear ANPs with existing super-resolution approaches (Supplementary Table 11). For example, the extreme nonlinearity and anti-Stokes luminescence should improve the achievable signal-to-noise and resolution limits of methods such as nonlinear structured illumination microscopy and near-infrared emission saturation[49] nanoscopy for a given photon budget[9,10]. Additionally, applying the photon localization accuracy concept to PASSI images (Fig. 4b), which already exhibit sub-100-nm resolution, yields a localization accuracy of <2 nm for only 7,600 collected photons, compared to the 10–40 nm accuracies typically achieved[8]. Realizing that the longer rise times might limit scan rates[50], we also calculated a multi-point excitation scheme (Supplementary Figs. 11–13) that suggests that possible scan rates of approximately 4 s or less per frame are achievable and reasonable using multi-point PASSI.

Finally, we note that in characterizing this PA system, we measure ~500–10,000-fold increases in emission intensity when the pump intensity is increased from the threshold (I_p^{th}) to twice the threshold value, which takes us beyond the steep-slope region of the ANP response curve (Figs. 2a, 3a). This enhancement, which we define as the parameter $\Delta_{av} = I_e(2I_p^{th})/I_e(I_p^{th})$, is substantially larger than in reported energy-looping systems (for example, $\Delta_{av} \leq 50$)[11,22] and suggests a simpler empirical method of identifying PA using a single measurable ratio. Δ_{av} captures the complex balance between R_2/R_1, cross-relaxation, and radiative versus non-radiative relaxation[7]. We find that all nanoparticles with ≥8% Tm^{3+} content reported here meet this criterion (Supplementary Table 9; with a maximum Δ_{av} value of ~10,000 attained with 20% Tm^{3+} ANPs, whereas a borderline value of ~500 is seen in the 100% Tm^{3+} ANPs, where the large increase in cross-relaxation rates leads to faster non-radiative depopulation of $^3H_4$ (ref. [46]).

In conclusion, we report steeply nonlinear nanomaterials, realizing PA in engineered nanocrystals at room temperature with continuous wave pumping. We observe that core–shell architectures doped with only Tm^{3+} ions exhibit avalanching behaviour for Tm^{3+} concentrations ≥8%,

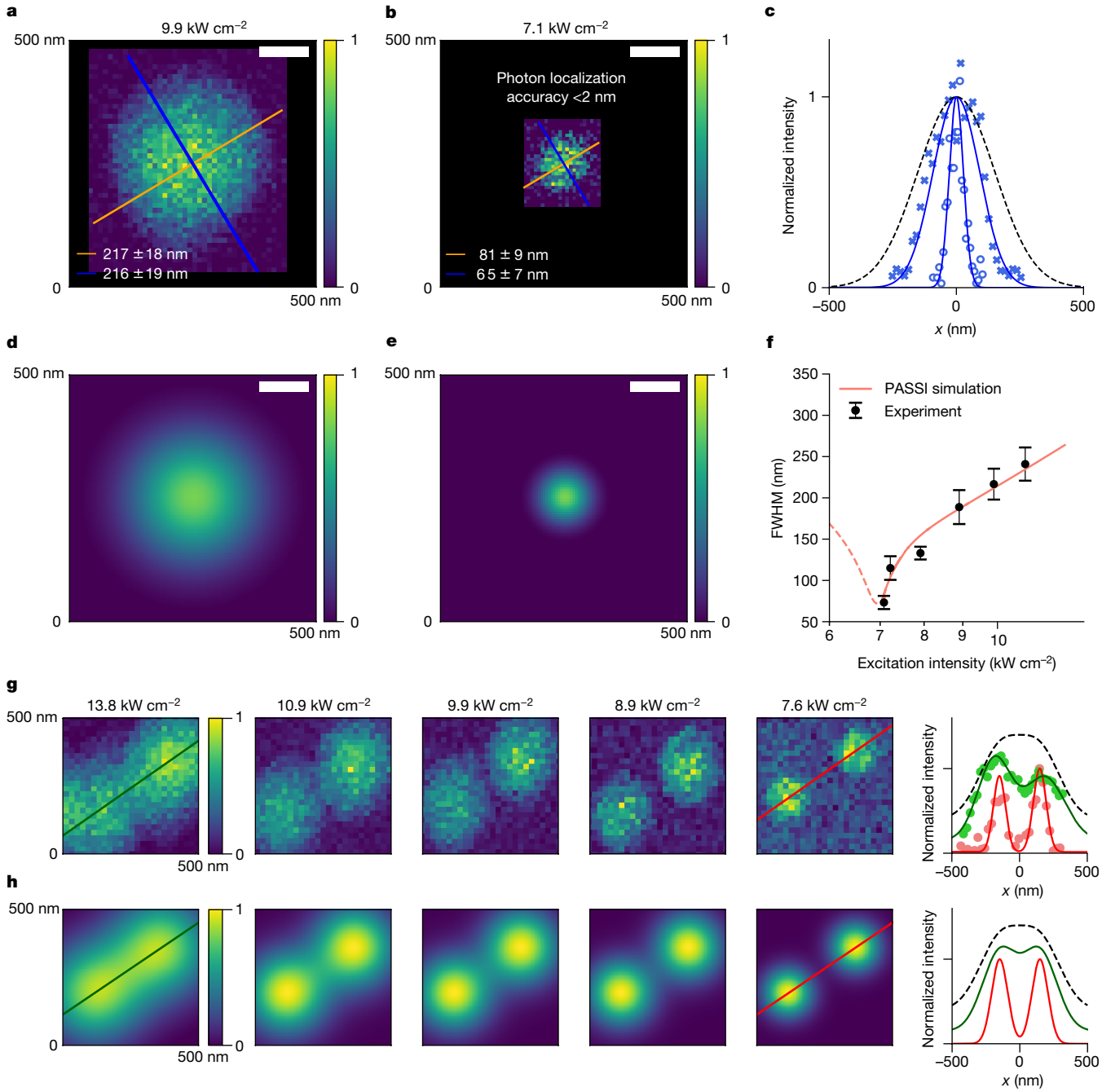

Fig. 4 | PA single-beam super-resolution imaging. a, **b**, Images of a single 8% Tm^{3+} ANP when excited in the saturation regime (9.9 kW cm^{-2}) (**a**) and in the PA regime (7.1 kW cm^{-2}) (**b**). **c**, Linecuts corresponding to the blue lines in **a** and **b**, with a linecut through a theoretical diffraction-limited focused Gaussian spot (for NA = 1.49, λ = 1,064 nm). **d**, **e**, Simulations of PASSI images for the same excitation intensities as in **a** and **b**, based on the measured emission–intensity curve shown in Fig. 3a (green crosses symbols), using the method developed in ref. [7]. **f**, measured (black) versus simulated (red) FWHMs of single-ANP PASSI images as a function of excitation intensity. Error bars are the root mean square of the standard deviations of Gaussian curve fittings of the two linecuts for each power in Supplementary Fig. 10. **g**, Experimental PASSI images of 8% Tm^{3+} ANPs, separated by 300 nm, excited at decreasing intensities, from near saturation (left) to near threshold (right). Linecuts from the colour-coded lines in the images, along with a linecut through a theoretical diffraction-limited image of linear emission from two emitters spaced by 300 nm (black dashed line) (far right). **h**, As in **g**, but for PASSI simulations. Scale bars are 100 nm.

and that the PA excitation threshold intensity is fully determined by the $^3F_4$ intermediate-state lifetime at higher concentrations. Further, we show that PA is achieved for excitation in the range 1,400–1,470 nm in addition to 1,064 nm. Along with emission intensities that scale nonlinearly with pump intensity up to the 26th power—enabling sub-70-nm SCM imaging resolution and <2-nm photon localization—these results can enable applications in local environmental, optical and chemical reporting and in super-resolution imaging.

Online content

Any methods, additional references, Nature Research reporting summaries, source data, extended data, supplementary information, acknowledgements, peer review information; details of author contributions and competing interests; and statements of data and code availability are available at https://doi.org/10.1038/s41586-020-03092-9.

1. Turcotte, D. L. Self-organized criticality. *Rep. Prog. Phys*. **62**, 1377–1429 (1999).
2. Ni, H. & Rand, S. C. Avalanche phase conjugation. *Opt. Lett*. **17**, 1222–1224 (1992).
3. Chivian, J. S., Case, W. E. & Eden, D. D. The photon avalanche: a new phenomenon in Pr^{3+}-based infrared quantum counters. *Appl. Phys. Lett*. **35**, 124–125 (1979).
4. Lenth, W. & Macfarlane, R. M. Excitation mechanisms for upconversion lasers. *J. Lumin*. **45**, 346–350 (1990).
5. Joubert, M.-F. Photon avalanche upconversion in rare earth laser materials. *Opt. Mater*. **11**, 181–203 (1999).
6. Auzel, F. Upconversion and anti-Stokes processes with f and d ions in solids. *Chem. Rev*. **104**, 139–174 (2004).
7. Bednarkiewicz, A., Chan, E. M., Kotulska, A., Marciniak, L. & Prorok, K. Photon avalanche in lanthanide doped nanoparticles for biomedical applications: super-resolution imaging. *Nanoscale Horiz*. **4**, 881–889 (2019).
8. Thompson, M. A., Lew, M. D. & Moerner, W. E. Extending microscopic resolution with single-molecule imaging and active control. *Annu. Rev. Biophys*. **41**, 321–342 (2012).
9. Gustafsson, M. G. L. Nonlinear structured-illumination microscopy: wide-field fluorescence imaging with theoretically unlimited resolution. *Proc. Natl Acad. Sci. USA* **102**, 13081 (2005).
10. Heintzmann, R. & Huser, T. Super-resolution structured illumination microscopy. *Chem. Rev*. **117**, 13890–13908 (2017).
11. Denkova, D. et al. 3D sub-diffraction imaging in a conventional confocal configuration by exploiting super-linear emitters. *Nat. Commun*. **10**, 3695 (2019).
12. Liu, Y. et al. Super-resolution mapping of single nanoparticles inside tumor spheroids. *Small* **16**, 1905572 (2020).
13. Marciniak, L., Bednarkiewicz, A. & Elzbieciak, K. NIR–NIR photon avalanche based luminescent thermometry with Nd^{3+} doped nanoparticles. *J. Mater. Chem. C* **6**, 7568–7575 (2018).
14. Pickel, A. D. et al. Apparent self-heating of individual upconverting nanoparticle thermometers. *Nat. Commun*. **9**, 4907 (2018).
15. Lay, A. et al. Optically robust and biocompatible mechanosensitive upconverting nanoparticles. *ACS Cent. Sci*. **5**, 1211–1222 (2019).
16. Xie, P. & Gosnell, T. R. Room-temperature upconversion fiber laser tunable in the red, orange, green, and blue spectral regions. *Opt. Lett*. **20**, 1014–1016 (1995).
17. Guy, S., Joubert, M. F. & Jacquier, B. Photon avalanche and the mean-field approximation. *Phys. Rev. B* **55**, 8240–8248 (1997).
18. Deng, H., Yang, S., Xiao, S., Gong, H.-M. & Wang, Q.-Q. Controlled synthesis and upconverted avalanche luminescence of cerium(III) and neodymium(III) orthovanadate nanocrystals with high uniformity of size and shape. *J. Am. Chem. Soc*. **130**, 2032–2040 (2008).
19. Wang, Q.-Q. et al. Highly efficient avalanche multiphoton luminescence from coupled Au nanowires in the visible region. *Nano Lett*. **7**, 723–728 (2007).
20. Ma, Z. et al. Origin of the avalanche-like photoluminescence from metallic nanowires. *Sci. Rep*. **6**, 18857 (2016).
21. Liu, Y. et al. Amplified stimulated emission in upconversion nanoparticles for super-resolution nanoscopy. *Nature* **543**, 229–233 (2017).
22. Levy, E. S. et al. Energy-looping nanoparticles: harnessing excited-state absorption for deep-tissue imaging. *ACS Nano* **10**, 8423–8433 (2016).
23. Fernandez-Bravo, A. et al. Continuous-wave upconverting nanoparticle microlasers. *Nat. Nanotechnol*. **13**, 572–577 (2018).
24. Si, X., Li, Z., Qu-Quan, W., Hong, D. & Shi-He, Y. Energy transfer and avalanche upconversion of $Nd_xY_{1-x}VO_4$ nanocrystals. *Chin. Phys. Lett*. **26**, 124209 (2009).
25. Bednarkiewicz, A. & Strek, W. Laser-induced hot emission in Nd^{3+}/Yb^{3+}:YAG nanocrystallite ceramics. *J. Phys. D* **35**, 2503–2507 (2002).
26. Dwivedi, Y., Bahadur, A. & Rai, S. B. Optical avalanche in Ho:Yb:Gd_2O_3 nanocrystals. *J. Appl. Phys*. **110**, 043103 (2011).
27. Wang, G., Peng, Q. & Li, Y. Luminescence tuning of upconversion nanocrystals. *Chemistry* **16**, 4923–4931 (2010).
28. Zhou, B., Shi, B., Jin, D. & Liu, X. Controlling upconversion nanocrystals for emerging applications. *Nat. Nanotechnol*. **10**, 924–936 (2015).
29. Tian, B. et al. Low irradiance multiphoton imaging with alloyed lanthanide nanocrystals. *Nat. Commun*. **9**, 3082 (2018).
30. Tajon, C. A. et al. Photostable and efficient upconverting nanocrystal-based chemical sensors. *Opt. Mater*. **84**, 345–353 (2018).
31. Bünzli, J.-C. G. & Piguet, C. Taking advantage of luminescent lanthanide ions. *Chem. Soc. Rev*. **34**, 1048–1077 (2005).
32. Gnach, A., Lipinski, T., Bednarkiewicz, A., Rybka, J. & Capobianco, J. A. Upconverting nanoparticles: assessing the toxicity. *Chem. Soc. Rev*. **44**, 1561–1584 (2015).
33. Gargas, D. J. et al. Engineering bright sub-10-nm upconverting nanocrystals for single-molecule imaging. *Nat. Nanotechnol*. **9**, 300 (2014).
34. Fischer, S., Bronstein, N. D., Swabeck, J. K., Chan, E. M. & Alivisatos, A. P. Precise tuning of surface quenching for luminescence enhancement in core–shell lanthanide-doped nanocrystals. *Nano Lett*. **16**, 7241–7247 (2016).
35. Johnson, N. J. J. et al. Direct evidence for coupled surface and concentration quenching dynamics in lanthanide-doped nanocrystals. *J. Am. Chem. Soc*. **139**, 3275–3282 (2017).
36. Liu, Q. et al. Single upconversion nanoparticle imaging at sub-10 W cm^{-2} irradiance. *Nat. Photon*. **12**, 548–553 (2018).
37. Chen, X. et al. Confining energy migration in upconversion nanoparticles towards deep ultraviolet lasing. *Nat. Commun*. **7**, 10304 (2016).
38. Wang, F. et al. Tuning upconversion through energy migration in core–shell nanoparticles. *Nat. Mater*. **10**, 968–973 (2011).
39. Gamelin, D. R., Lüthi, S. R. & Güdel, H. U. The role of laser heating in the intrinsic optical bistability of Yb^{3+}-doped bromide lattices. *J. Phys. Chem. B* **104**, 11045–11057 (2000).
40. Butcher, J. C. *Numerical Methods for Ordinary Differential Equations* (Wiley, 2016).
41. Goldner, P. & Pelle, F. Photon avalanche fluorescence and lasers. *Opt. Mater*. **5**, 239–249 (1996).
42. Joubert, M. F., Guy, S. & Jacquier, B. Model of the photon-avalanche effect. *Phys. Rev. B* **48**, 10031–10037 (1993).
43. Hong, G. et al. Through-skull fluorescence imaging of the brain in a new near-infrared window. *Nat. Photon*. **8**, 723–730 (2014).
44. Ostrowski, A. D. et al. Controlled synthesis and single-particle imaging of bright, sub-10 nm lanthanide-doped upconverting nanocrystals. *ACS Nano* **6**, 2686–2692 (2012).
45. Hossan, M. Y. et al. Explaining the nanoscale effect in the upconversion dynamics of β-$NaYF_4$:Yb^{3+}, Er^{3+} core and core–shell nanocrystals. *J. Phys. Chem. C* **121**, 16592–16606 (2017).
46. Teitelboim, A. et al. Energy transfer networks within upconverting nanoparticles are complex systems with collective, robust, and history-dependent dynamics. *J. Phys. Chem. C* **123**, 2678–2689 (2019).
47. Chan, E. M., Gargas, D. J., Schuck, P. J. & Milliron, D. J. Concentrating and recycling energy in lanthanide codopants for efficient and spectrally pure emission: the case of $NaYF_4$:Er^{3+}/Tm^{3+} upconverting nanocrystals. *J. Phys. Chem. B* **116**, 10561–10570 (2012).
48. Corle, T. R. & Kino, G. S. *Confocal Scanning Optical Microscopy and Related Imaging Systems* (Academic Press, 1996).
49. Chen, C. et al. Multi-photon near-infrared emission saturation nanoscopy using upconversion nanoparticles. *Nat. Commun*. **9**, 3290 (2018).
50. Pichaandi, J., Boyer, J.-C., Delaney, K. R. & van Veggel, F. C. J. M. Two-photon upconversion laser (scanning and wide-field) microscopy using Ln^{3+}-doped $NaYF_4$ upconverting nanocrystals: a critical evaluation of their performance and potential in bioimaging. *J. Phys. Chem. C* **115**, 19054–19064 (2011).

Methods

Materials

Sodium trifluoroacetate (Na-TFA, 98%), sodium oleate, ammonium fluoride (NH_4F), yttrium chloride (YCl_3, anhydrous, 99.99%), thulium chloride ($TmCl_3$, anhydrous, >99.9%), gadolinium chloride ($GdCl_3$, anhydrous, 99.99%), yttrium trifluoroacetate (>99.99%), oleic acid (OA, 90%) and 1-octadecene (ODE, 90%) were purchased from Sigma-Aldrich.

Synthesis of core ANPs

The synthesis of $NaY_{1-x}Tm_xF_4$ ANP cores with average diameters ranging from $d = 10$ nm to 18 ± 1 nm (see Supplementary Table 1) was based on reported procedures[44]. For the case of $x = 0.01$ (meaning 1% Tm^{3+} doping), YCl_3 (0.99 mmol, 193.3 mg) and $TmCl_3$ (0.01 mmol, 2.8 mg) were added into a 50-ml three-neck flask, followed by an addition of 6 ml OA and 14 ml ODE. The solution was stirred under vacuum and heated to 100 °C for 1 h. During this time, the solution became clear. After that, the flask was subjected to three pump–purge cycles, each consisting of refilling with N_2 and immediately pumping under vacuum to remove water and oxygen. Afterwards, sodium oleate (2.5 mmol, 762 mg) and NH_4F (4 mmol, 148 mg) were added to the flask under N_2 flow. Subsequently, the resealed flask was placed under vacuum for 15 min at 100 °C, followed by three pump–purge cycles. Subsequently, the flask was quickly heated from 100 °C to 320 °C (the approximate ramp rate was 25 °C min^{-1}). The temperature was held at 320 °C for 40–60 min, after which the flask was rapidly cooled to room temperature using a stream of compressed air.

To isolate the nanoparticles, ethanol was added to the solution in a 1:1 volume ratio, and the precipitated nanoparticles were isolated by centrifugation (5 min at 4,000 rpm). The pellet was suspended in hexanes and centrifuged to remove large and aggregated particles. The nanoparticles remaining in the supernatant were washed two additional times by adding ethanol, isolating by centrifugation and dissolving the pellet in hexanes. The nanoparticles were stored in hexanes with two drops of oleic acid to prevent aggregation.

Shell growth

A 0.1 M stock solution of 20% $GdCl_3$ and 80% YCl_3 was prepared by adding YCl_3 (2 mmol, 390.5 mg), $GdCl_3$ (0.5 mmol, 131.8 mg), 10 ml OA and 15 ml ODE to a 50-ml three-neck flask. The solution was stirred and heated to 110 °C under vacuum for 30 min. After that, the flask was filled with N_2 and heated to 200 °C for about 1 h, until the solution became clear and no solid was observed in the flask. Subsequently, the flask was cooled to 100 °C and placed under vacuum for 30 min. A 0.2 M solution of Na-TFA was prepared by stirring Na-TFA (4 mmol, 544 mg), 10 ml OA and 10 ml ODE in a flask under vacuum at room temperature for 2 h, ensuring that all chemicals were dissolved. Using a nanoparticle synthesis robot, the Workstation for Automated Nanocrystal Discovery and Analysis (WANDA), 3–9 nm $NaY_{0.8}Gd_{0.2}F_4$ shells (see Supplementary Table 1) were grown on ANP cores using a layer-by-layer protocol similar to that deployed in Levy et al.[22]. Briefly, for a shell thickness of 3 nm, 6 ml ODE and 4 ml OA were added to the dried ANP cores and heated to 280 °C at 20 °C min^{-1} in the WANDA glove box. The automated protocol alternated between injections of a 0.2 M Na-TFA stock solution and a 0.1 M stock solution of 20% gadolinium and 80% yttrium oleate solution. One injection was performed every 20 min for a total of 12 injections (6 injections for each precursor). Following the last injection, each reaction was annealed at 280 °C for an additional 30 min and then cooled rapidly by nitrogen flow. The particles were isolated and purified according to the purification protocol described for ANP cores.

Core–shell $NaYF_4$ nanoparticles doped with Tm^{3+} (1–100%) were synthesized using analogous methods.

Nanoparticle characterization

Transmission electron microscopy (TEM) was performed using a JEOL JEM-2100F field-emission TEM system at an acceleration voltage of 200 kV, a FEI Themis 60-300 STEM/TEM operating at an acceleration voltage of 300 kV and a Tecnai T20 S-TWIN TEM operating at 200 kV with a LaB_6 filament. Size statistics were acquired for approximately 100 nanoparticles using ImageJ software. X-ray diffraction measurements were performed using a Bruker D8 Discover diffractometer with Cu Kα radiation. The average core diameter and shell sizes are given in Fig. 3a. We note that the larger cores are slightly prolate in shape (Supplementary Fig. 2).

Preparation of nanocrystal film samples

Nanoparticles (40 µl of a 1 µM suspension in hexane) were either drop-cast or spin-coated on a coverslip. Atomic force microscopy measurements (Bruker Dimension AFM) were performed to measure the thicknesses of the films.

Optical characterization of ANPs

For single-ANP imaging, a dilute dispersion of nanoparticles was deposited on a glass coverslip and placed on an inverted confocal microscope (Nikon, Eclipse Ti-S inverted microscope). A 1,064-nm continuous-wave diode laser (Thorlabs, FELH 750) or a Ti-sapphire pulsed laser (Coherent, Chameleon OPO Vis, 1,390–1,510 nm, 80 MHz) were directed into the back aperture of an NA = 1.49 100× immersion-oil objective (Olympus) and focused directly onto the sample on an three-dimensional (XYZ) nanoscanning piezo stage (Physik Instrumente, P-545.xR8S Plano).

For measurements on film samples, an NA = 0.95 100× air objective lens (Nikon) was used. Emitted light was collected back through the same objective, filtered by 850-nm short-pass (Thorlabs, FESH 850) and 750-nm long-pass (Thorlabs, FELH 750) filters, and sent to a spectrometer equipped with an electron-multiplying charge-coupled device (Princeton Instruments, ProEM: 1600^2 eXcelon3) or a single-photon avalanche diode (Micro Photon Device, PDM series). For power dependence measurements, a neutral density wheel with a continuously variable density was used, synchronized with the collection system and automatically rotated by an Arduino-controlled rotator. Powers were simultaneously recorded by a Thorlabs power meter by using a glass coverslip to reflect ~10% of the incoming flux. Average excitation power densities were calculated using measured laser powers and the $1/e^2$ area calculated from the imaged laser spot.

Time-resolved photoluminescence

Samples were excited with a diode laser (Thorlabs) modulated at frequencies from 0.5 Hz to 5 Hz by a function generator (Stanford Research Systems DS345). Emitted light collected by the NA = 0.95 100× objective (Nikon) was detected by a single-photon avalanche diode (Micro Photon Device, PDM series). A time-correlated single-photon counting device (Picoquant, Hydraharp 400) was used to record the timing data.

PA mechanism in our ANPs

As discussed in the main text, a single GSA event in lanthanide-based PA initiates a chain reaction of ESA and cross-relaxation events between Ln^{3+} ions, resulting in the emission of many upconverted photons. This mechanism amplifies the population of excited states, such as the 800-nm-emitting Tm^{3+} $^3H_4$ level (Fig. 1c), through a positive-feedback loop of ESA from an intermediate state ($^3F_4$), followed by cross-relaxation (an energy-transfer process) back down to the same intermediate state while promoting a second ground-state Tm^{3+} ion up to its intermediate state (we note that the cross-relaxation process is accompanied by the emission of phonons to compensate an energy mismatch of about 1,200 cm^{-1}). This process can effectively double the $^3F_4$ population on every iteration of the loop, and the repeated looping results in nonlinear amplification of excited-state populations.

The ESA is effective because the absorption peak for the electronic $^3F_2$–$^3F_4$ transition is close to the 1,064-nm excitation wavelength. However, the 1,064-nm photons have an energy mismatch of ~1,200 cm^{-1} for the electronic $^3H_6$–$^3H_5$ transition, which decreases the GSA

cross-section at that wavelength. Owing to the energetic mismatch, GSA is a phonon-assisted process in this case, which makes its oscillator strength very small, ~10^4 times weaker than for excitation resonant with the purely electronic *f*–*f* transitions.

Materials considerations for achieving PA in nanoparticles

PA was first observed at low temperatures—as is often the case—although several room-temperature demonstrations have been reported in bulk systems (for example, refs. [5–7,18,51–55]). In nanomaterials, however, the sensitivity of Ln^{3+} photophysics to local material properties has precluded the realization of PA and has hindered room-temperature operation.

As noted in the main text, four key features were combined to design nanocrystals that may be capable of PA. The first is the recent design paradigm for Ln^{3+}-based upconverting nanoparticles, in which high Ln^{3+} content, engineered energy confinement and reduced surface losses result in exceptional efficiencies and brightness[23,29,33–37,56]. A second feature is the choice of Tm^{3+} (Fig. 1a), an ion with a particularly slow intermediate-state decay rate W_2, which strongly influences PA behaviour[5–7] (see below). The third critical aspect exploits the compositional strategy employed previously for energy-looping nanoparticles[22], in which typical Yb^{3+} sensitizers are omitted and high concentrations of Tm^{3+} ions are doped into a β-phase $NaYF_4$ matrix, enhancing Tm^{3+}–Tm^{3+} cross-relaxation and ESA while reducing GSA (Fig. 1). The fourth key element, also shared with energy-looping nanoparticles, is the selection of excitation wavelengths in the NIR-II transparency window (either 1,064 nm or 1,450 nm; Fig. 1), which are optimized for resonant ESA while maintaining non-resonant GSA, in contrast to the usual wavelengths used for pumping Tm^{3+} (800 nm, or 980 nm when combined with Yb^{3+} sensitization; Fig. 1)[6,11,12,21,38].

To determine whether these design criteria enable nanocrystals to host PA, we synthesized Tm^{3+}-doped β-$NaYF_4$ core–shell structures 16–33 nm in total diameter[29,33]. As described in Methods sections 'Synthesis of core ANPs' and 'Shell growth', the Tm^{3+}-doped core in each ANP is surrounded by an optically inert shell to minimize surface losses[33] (Figs. 1, Supplementary Figs. 1, 2 and Supplementary Tables 1, 2). These nanoparticles may be excited in the NIR-II region to emit in the NIR-I region at 800 nm (ref. [22]). Both spectral windows are valuable for imaging with limited photodamage through living systems or scattering media[57]. More generally, the near-infrared operation and exceptional photostability, along with the unique combination of steep nonlinearity and efficiency offered by PA suggest the utility of ANPs in a diverse array of applications, including sub-wavelength bioimaging[7,11,12], photonics and light detection[56–58], temperature[13,14,59] and pressure[15] transduction, neuromorphic computing[60] and quantum optics[61,62].

Data availability

All data generated or analysed during this study, which support the plots within this paper and other findings of this study, are included in this published article and its Supplementary Information. Source data are provided with this paper.

Code availability

The code for modelling the PA behaviour using the differential rate equations described in the Supplementary Information are freely available at https://github.com/nawhgnahc/Photon_Avalanche_DRE_calculation.git.

51. Auzel, F., Chen, Y. & Meichenin, D. Room temperature photon avalanche up-conversion in Er-doped ZBLAN glass. *J. Lumin.* **60-61**, 692–694 (1994).
52. Auzel, F. & Chen, Y. Photon avalanche luminescence of Er^{3+} ions in $LiYF_4$ crystal. *J. Lumin.* **65**, 45–56 (1995).
53. Gomes, A. S. L., Maciel, G. S., de Araújo, R. E., Acioli, L. H. & de Araújo, C. B. Diode pumped avalanche upconversion in Pr^{3+}-doped fibers. *Opt. Commun.* **103**, 361–364 (1993).
54. Martín, I. R. et al. Room temperature photon avalanche upconversion in Tm^{3+}-doped fluoroindate glasses. *J. Phys. Condens. Matter* **12**, 1507–1516 (2000).
55. Li, Y. et al. BiOCl:Er^{3+} nanosheets with tunable thickness for photon avalanche phosphors. *ACS Appl. Nano Mater.* **2**, 7652–7660 (2019).
56. Garfield, D. J. et al. Enrichment of molecular antenna triplets amplifies upconverting nanoparticle emission. *Nat. Photon.* **12**, 402–407 (2018).
57. Liu, Y. et al. Controlled assembly of upconverting nanoparticles for low-threshold microlasers and their imaging in scattering media. *ACS Nano* **14**, 1508–1519 (2020).
58. Fernandez-Bravo, A. et al. Ultralow-threshold, continuous-wave upconverting lasing from subwavelength plasmons. *Nat. Mater.* **18**, 1172–1176 (2019).
59. Kilbane, J. D. et al. Far-field optical nanothermometry using individual sub-50 nm upconverting nanoparticles. *Nanoscale* **8**, 11611–11616 (2016).
60. Zhai, Y. et al. Near infrared neuromorphic computing via upconversion-mediated optogenetics. *Nano Energy* **67**, 104262 (2020).
61. Bradac, C. et al. Room-temperature spontaneous superradiance from single diamond nanocrystals. *Nat. Commun.* **8**, 1205 (2017).
62. Asenjo-Garcia, A., Kimble, H. J. & Chang, D. E. Optical waveguiding by atomic entanglement in multilevel atom arrays. *Proc. Natl Acad. Sci. USA* **116**, 25503 (2019)

Acknowledgements P.J.S., Y.D.S., S.H.N. and C.L. gratefully acknowledge support from the Global Research Laboratory (GRL) Program through the National Research Foundation of Korea (NRF) funded by the Ministry of Science and ICT (number 2016911815), and KRICT (KK2061-23, SKO1930-20). Y.D.S. acknowledges the Industrial Strategic Technology Development Program (number 10077582) funded by the Ministry of Trade, Industry, and Energy (MOTIE), Korea. E.Z.X. gratefully acknowledges support from the NSF Graduate Research Fellowship Program. Y.L. was supported by a China Scholarship Council fellowship. A.T. was supported by the Weizmann Institute of Science – National Postdoctoral Award Program for Advancing Women in Science. Work at the Molecular Foundry was supported by the Office of Science, Office of Basic Energy Sciences, of the US Department of Energy under contract number DE-AC02-05CH11231. K.Y. acknowledges support from Programmable Quantum Materials, an Energy Frontier Research Center funded by the US Department of Energy (DOE), Office of Science, Basic Energy Sciences (BES), under award DE-SC0019443. A.B. acknowledges financial support from NCN, Poland, grant number UMO-2018/31/B/ST5/01827.

Author contributions P.J.S., E.M.C., B.E.C., C.L. and Y.D.S. conceived the study. Experimental measurements and associated analyses were conducted by C.L., E.Z.X., Y.L., A.T., K.Y., A.F.-B., S.H.N. and E.M.C. Advanced nanoparticle synthesis and characterization was performed by Y.L., A.T. and E.M.C. Theoretical modelling and simulations of PA photophysics were carried out by C.L., E.M.C., A.T., A.M.K. and A.B. Advanced simulations of super-resolution imaging were performed by A.M.K. and A.B. All authors contributed to the preparation of the manuscript.

Competing interests The authors declare no competing interests.

Additional information

Supplementary information is available for this paper at https://doi.org/10.1038/s41586-020-03092-9.

Correspondence and requests for materials should be addressed to Y.D.S., A.B., B.E.C., E.M.C. or P.J.S.

Peer review information *Nature* thanks Xueyuan Chen, Andries Meijerink and the other, anonymous, reviewer(s) for their contribution to the peer review of this work. Peer reviewer reports are available.